# 12

# Characterization of Hepatic Lesions Using Grid Computing (Globus) and Neural Networks

Sheng Hung Chung[1] and Ean Teng Khor[2]
*School of Science and Technology, Wawasan Open University, Penang, Malaysia*

## 1. Introduction

Magnetic Resonance Imaging (MRI) images have been widely used for liver disease diagnosis. Designing and developing computer-assisted image processing techniques to help doctors improve their diagnosis has received considerable interest over the past years. In this paper, a computer-aided diagnostic (CAD) system for the characterization of hepatic lesions, specifically cyst and tumor as well as healthy liver, from MRI images using texture features and implementation of grid computing (Globus approach) and neural networks (NN) is presented. Texture analysis is used to determine the changes in functional characteristics of organs at the onset of a liver disease, Region of interest (ROI) extracted from MRI images are used as the input to characterize different tissue, namely liver cyst and healthy liver using first-order statistics. The results for first-order statistics are given and their potential applicability in grid computing is discussed. The measurements extracted from First-order statistic include entropy and correlation achieved obvious classification range in detecting different tissues in this work.

In this chapter, texture analysis of liver MRI images based on the Spatial Grey Level Co-occurrence Matrix (SGLCM) [3] is proposed to discriminate normal, malignant hepatic tissue (i.e. liver tumor) and cysts in MRI images of the abdomen. SGLCM, also known as Grey Tone Spatial Dependency Matrix [3], is a tabulation of how often different combinations of pixel brightness values (i.e. grey-level) occur in an image. Regions of interest (ROI) from cysts, tumor and healthy liver were used as input for the SGLCM calculation. Second order statistical texture features estimated from the SGLCM are then applied to a Feed-forward Neural Network (FNN) and Globus toolkit for the characterization of suspected liver tissue from MRI images for hepatic lesions classification. This project proposed an automated distributed processing framework for high-throughput, large-scale applications targeted for characterization of liver texture statistical measurements mainly healthy liver, fatty liver, liver cyst for MRI (Magnetic Resonance Imaging) images.

Table 1 lists eight second-order statistical calculations based on SGLCM, namely, contrast, entropy, correlation, homogeneity, cluster tendency, inverse difference moment, energy, and angular second moment, which have shown useful results in hepatic lesions classification for liver tumor using Computed Tomography (CT), Ultrasonography (US) and

| Properties | Valanis [4] | CHEN [5] | MIR [6] | MOUGIAKAKOU [7] |
|---|---|---|---|---|
| Contrast | √ | | | √ |
| Entropy | | √ | √ | √ |
| Correlation | √ | √ | √ | √ |
| Homogeneity | | | √ | √ |
| Cluster Tendency | √ | | | |
| Inverse Difference Moment | √ | | | √ |
| Energy | √ | | √ | √ |
| Angular Second Moment | √ | √ | | |

Table 1. SGLCM properties for second-order statistical measurements. The features successfully examined in prior work are summarized in Table 1 below.

MRI. The measurements identified in various approaches are indicated by a tick. The SGLCM approach undertaken by Valanis et al. [4] was to classify three hepatic tissues: normal, hemangeoma and hepatocellular carcinoma on CT images with a resolution of 512 X 512 pixels and 8 bits per pixel (bpp) (256 grey levels). Correlation, inverse difference moment and cluster tendency were shown in the paper to achieve classification rates of up to 90.63% after being applied with feature selection based on a Genetic Algorithm (GA) approach. Of particular interest is an approach by Chen [5], using a modified probabilistic neural network (MPNN) to classify liver tumor, hepatoma and hemangeoma on CT images with 12 bpp representing 4096 grey levels and resolution of 320 X 320 pixels. The entropy and correlation showed better performance than other features extracted from co-occurrence matrices at directions $\theta = 0°, 45°, 90°$ and 135°, resulting in a classification rate of 83% where the misclassification resulted from the tumor matrices block size. The classification rate could be increased by reducing the block size. Another approach was by Mir [6] to classify normal and malignant liver on 256 X 256 pixels CT images. Entropy and local homogeneity were found to be consistent within a class and most appropriate for discrimination of the malignant and normal liver. Mougiakakou [7] implemented an automated CAD system for characterization of liver CT images into cysts, hepatoma and hemangeoma using a multiple NN classification scheme. Contrast, entropy, correlation and homogeneity were the identified features based on feature selection using the Squared Mahalanobis Distance as the fitness function [8].

### 1.1 Image acquisition

MRI produces images of the insides of the body. Unlike an X-ray, MRI does not use radiation. Instead, a magnetic field is used to make the body's cells vibrate [1]. The vibrations give off electrical signals which are interpreted and turned into very detailed images of "slices" of the body. MRI may be used to make images of every part of the body, including the bones, joints, blood vessels, nerves, muscles and organs. Different types of tissue show up in different grayscale intensities on a computer-generated image. In this study, series of MRI images were acquired from the Diagnostic Imaging Department of Selayang Hospital, Malaysia, using a Siemens Magnetom Avanto, 1.5T MRI Scanner. The sample liver MRI images (256 X 256 pixels, 12 bps) were acquired consisting of sets of cyst, liver tumor and healthy liver, for training and testing.

## 2. Grid computing with globus

Grid Computing describes computation in which jobs are run on a distributed computational unit spanning two or more administrative domains. It has sparked tremendous excitement among scientists worldwide and has renewed the interest of the scientific community toward distributed computing, an area which was almost forgotten during the 90's.

The Globus toolkit [4] was created in the late 1990s as part of a joint research project between Argonne National Laboratory and the Information Sciences Institute at the University of Southern California. Its aim was to provide a solution to the computational needs of large virtual organizations [4] that span multiple institutional and administrative domains. Globus is a middleware toolkit that provides fundamental distributed computing services such as authentication, job starting and resource discovery.

Globus provides a collection of services [5] including: GSI, Grid Security Infrastructure which provides authentication based on a Certificate Authority trust model; GRAM, Grid Resource Allocation Manager which handles job starting or submission; GridFTP, providing extensions to the FTP standard to provide GSI authentication and high performance transfer; MDS, Monitoring and Discovery Service enabling remote resource discovery.

By itself Globus does not provide all of the tools and services required to implement a full featured distributed computing environment. Additional tools are available to fill some of the gaps. The National Center for Supercomputing Applications (NCSA) provides a patch to add GSI authentication to OpenSSH. This allows Globus environments to have terminal based single-signon. Globus does not provide any scheduling functionality, but rather relies on the client operating system scheduler or batch schedulers such as OpenPBS [6] to handle local scheduling activities.

Global scheduling between Globus processes can be provided by meta-schedulers, such as Condor-G [6]. Condor-G submits jobs to the GRAM service running on Globus nodes and GRAM handles the task of submitting the job to the local scheduling system.

## 3. Spatial grey level co-occurrence matrices

The SGLCM aspect of texture is concerned with the spatial distribution and spatial dependence among the grey levels in a local area. This concept was first used by Julesz [9] in texture discrimination experiments. Being one of the most successful methods for texture discrimination at present, we have investigated its effectiveness for use with MRI images in the present work. This method is based on the estimation of the second order joint conditional probability density function [10]

$$f(i,j \mid d,\theta) \tag{1}$$

where $\theta$ = 0°, 45°, 90°, 135°, 180°, 225°, 270°, and 315°.Each $f(i,j \mid d,\theta)$ *i*s the probability of going from grey level $i$ to grey level $j$, given that the inter-sample spacing is $d$ and the direction is given by the angle $\theta$. The estimated value for these probability density functions can thus be written in matrix form [11]

$$\phi(d,\theta) = [f(i,j,\mid d,\theta)] . \tag{2}$$

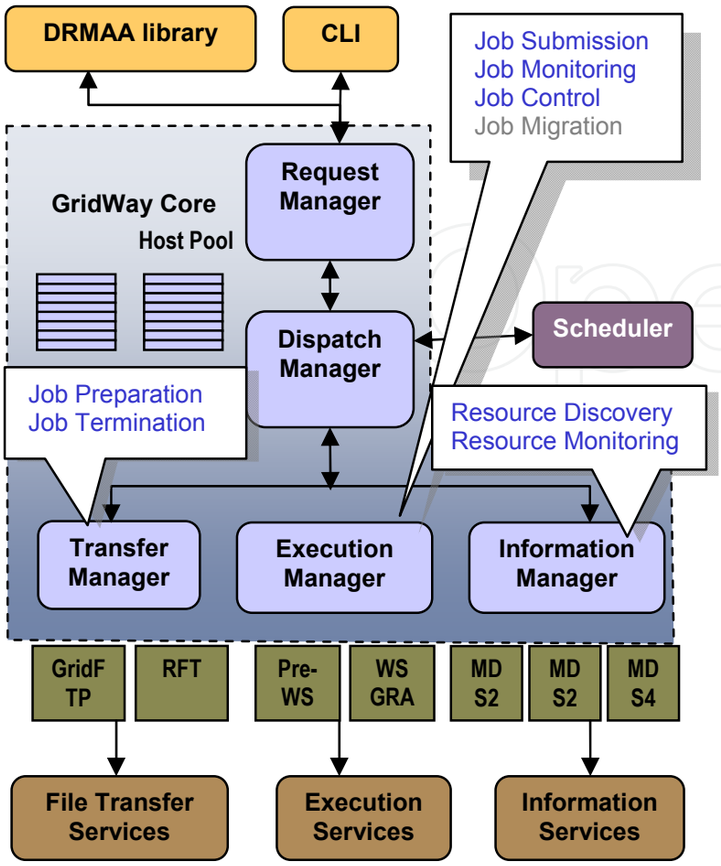


Fig. 1. Component of Gridway in Globus

For computing these probability distribution functions, scanning of the image in four directions has been carried out in this work, with $\theta$ = 0°, 45°, 90° and 135° sufficient, since the probability density matrix for the rest of the directions can be computed from these four basic directions, as denoted in the following [11]

$$\phi(d,0) = \phi^t(\mathrm{d},180)$$

$$\phi(d,45) = \phi^t(\mathrm{d},225)$$

$$\phi(d,90) = \phi^t(\mathrm{d},270)$$

$$\phi(d,135) = \phi^t(\mathrm{d},315) \tag{3}$$

where $\phi^t(\mathrm{d},\theta)$ denotes the transpose of the matrix for the inter-sample spacing $d$, and direction, $\theta$.

### 3.1 Second-order statistical measurements

Findings by other researchers on SGLCM second-order feature extraction for use in statistical classification using neural networks (NN) has been shown to be efficient and very

effective [4-7]. There are eleven general second-order statistic measurements, as illustrated in [12], which include energy, entropy, contrast, correlation, homogeneity, inverse different moment, inertia, skewness, kurtosis, angular second moment and cluster tendency. The second-order statistical measurements commonly used in most texture classification cases for hepatic tissues using SGLCM are energy, entropy, homogeneity, inertia, contrast and correlation.

Entropy is a notoriously difficult term to understand shown as follows[10].

$$H(S_\theta(d)) = \sum_{i=0}^{NG-1} \sum_{j=0}^{NG-1} S_\theta(i,j,d) \log S_\theta(i,j,d) \tag{4}$$

where $S_\theta(i,j,d)$ is the *(i, j)*th entry in a co-occurrence matrix, *NG* is the number of grey levels in the image from which the SGLCM matrices are extracted.

The concept of entropy comes from thermodynamics, referring to the quantity of energy that is permanently lost to heat ("chaos") every time a reaction or a physical transformation occurs. Entropy cannot be recovered to do useful work. Because of this, the term is used in non-technical speech to mean irremediable chaos or disorder. Also, as with Angular Second Moment [11], the equation used to calculate physical entropy is very similar to the one used for the texture measure. In image processing, entropy measures the disorder or randomness in an image. The smaller the value of entropy, $H(S_\theta(d))$ , the less common is the occurrence of the pixel combinations [12]. Entropy measures the randomness of the elements of the matrix when all elements of the matrix are maximally random, entropy has its highest value. So, a homogeneous image has lower entropy than an inhomogeneous image.

Energy, the opposite of entropy, is, in this context denoted by.

$$E(S_\theta(d)) = \sum_{i=0}^{NG-1} \sum_{j=0}^{NG-1} [S_\theta(i,j)d]^2 \tag{5}$$

The energy of a texture describes the uniformity of the texture. In a homogeneous image there are very few dominant grey-tone transitions, hence the co-occurrence matrix of this image will have fewer entries of large magnitude. So, the energy of an image is high when the image is homogeneous. In that sense, it represents orderliness. Thus, energy is useful for measuring the texture orderness in the image.

Homogeneity is the dissimilarity and contrast result in larger numbers for more contrasty windows,

$$L(S_\theta(d)) = \sum_{i=0}^{NG-1} \sum_{j=0}^{NG-1} \frac{1}{1+(i-j)^2} S_\theta(i,j,d) \tag{6}$$

If weights decrease away from the diagonal, the result will be larger for images with little contrast. Homogeneity weights values by the inverse of the contrast weight, with weights decreasing exponentially away from the diagonal. When there is a large amount of contrast, weights are created in SGLCM so that the calculation results in a larger figure. Values on the SGLCM diagonal show contrast as follows,

$$Con(S_\theta(d)) = \sum_{i=0}^{NG-1} \sum_{j=0}^{NG-1} (i-j)^2 S_\theta(i,j,d,\theta) \tag{7}$$

For non-square matrices, the correlation function computes the linear Pearson correlation coefficient of two vectors or the correlation matrix of an *i* x *j* array,

$$C(S_\theta(d)) = \frac{\sum_{i=0}^{NG-1} \sum_{j=0}^{NG-1} (i-\mu_i)(j-\mu_j) S_\theta(i,j,d,\theta)}{\mu_i \mu_j} \tag{8}$$

where $\mu$ refers to the mean intensity value of the image in the x and y directions, respectively,

$$\mu_i = \sum_{i=0}^{NG-1} i \sum_{j=0}^{NG-1} S_\theta(i,j) \tag{9}$$

$$\mu_j = \sum_{i=0}^{NG-1} j \sum_{j=0}^{NG-1} S_\theta(i,j) \tag{10}$$

When correlation is high, the image will be more complex than when correlation is low. If vectors of unequal lengths are specified, the longer vector is truncated to the length of the shorter vector and a single correlation coefficient is returned. If an *i* x *j* array is specified, the result will be an *i* x *j* array of linear Pearson correlation coefficients, with the element *i,j* corresponding to correlation of the *i*th rows and *j*th column of the input array.

The inverse difference moment is defined as ,

$$IDM(S_\theta(d)) = \sum_{i=0}^{NG-1} \sum_{j=0}^{NG-1} \frac{1}{1+(i-j)^2} S_\theta(i,j,d,\theta) \tag{11}$$

It has a relatively high value when the high values of the matrix are near the main diagonal because the squared difference $(i, j)^2$ is then smaller, which increases the value of $\frac{1}{1+(i-j)^2}$.

The feature inertia defined as

$$I(S_\theta(d)) = \sum_{i=0}^{NG-1} \sum_{j=0}^{NG-1} (i-j)^2 S_\theta(i,j,d,\theta) \tag{12}$$

which gives the opposite effect as the inverse difference moment does; when the high values of the matrix are further away from the main diagonal, the value of inertia becomes higher.

So inertia and the inverse difference moment are measures for the distribution of grey values in the image.

The skewness feature, also known as cluster shade and cluster prominence, is the measure of the skewness of the matrix [10]

$$S(S_\theta(d)) = \sum_{i=0}^{NG-1} \sum_{j=0}^{NG-1} (i-\mu_i)^3 (j-\mu_j)^3 S_\theta(i,j,d) \tag{13}$$

When cluster shade and cluster prominence are high, the image is asymmetric.

## 4. Implementation of SGLCM, globus for hepatic lesions detection using region of interest

In constructing the sparse coding for SGLCM, the reduction of the number of intensity levels by quantizing the image to fewer levels of intensity [13] helps increase the speed of computation, with some loss of textural information. An interactive graphical user interface (GUI) region drawing tool was developed for image block size flexibility. Inter-sample distance of $d$ = 1, image block size of 12 x 12 pixels and direction $\theta$= 0°, 45°, 90° and 135°, were used in the experiment. Fig. 2 shows an ROI drawn on healthy liver texture for NN training. Fig. 3 and Fig. 4 show the ROI image block of 12 x 12 pixels drawn on suspected texture areas of cyst and liver tumor, respectively.

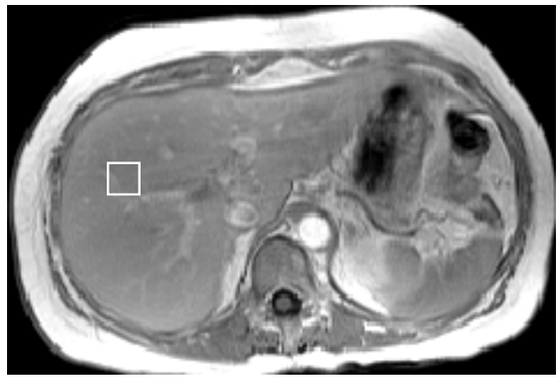

Fig. 2. 12 x 12 ROI block drawn on healthy liver in a MR image of the abdomen.

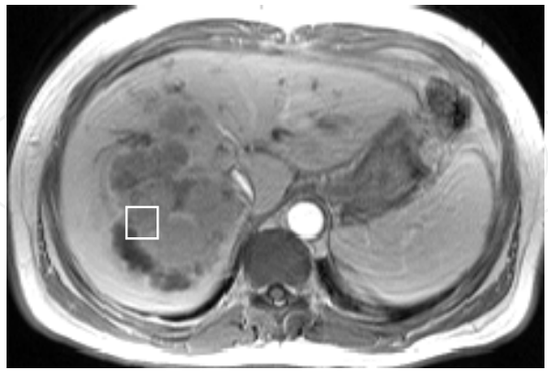

Fig. 3. 12 x 12 ROI block drawn on suspected liver tumor in a MR image of the abdomen. Liver tumor has irregular shape and has multiple growths tissue.

Co-occurrence matrices for the $\theta$ = 0° and $\theta$ = 90° are calculated as illustrated in Fig. 5 and Fig. 6, respectively. A test image of 4 x 4 pixels was used as the input to illustrate the sparse matrix construction. As observed in Fig. 4, each pixel within the test image window becomes

the reference pixel in the position of the matrix, starting from the upper left corner and proceeding to the lower right. The pixels along the right edge of the image have no right hand neighbour, so they are not used in this count.

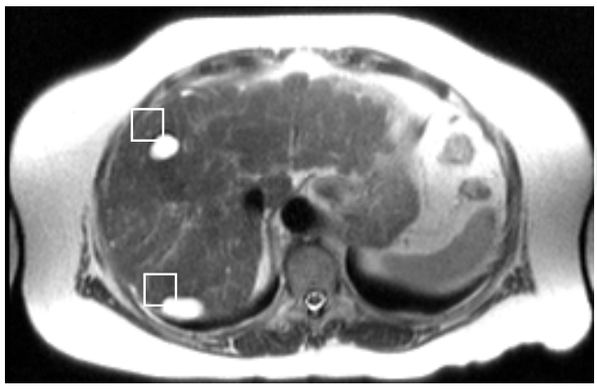

Fig. 4. 12 x 12 ROI block drawn on cyst in a MR image of the abdomen. cyst is a recently recognized genetic disorder characterized by the appearance of numerous cysts spread throughout the liver. A cyst may be identified as an abnormal fluid-filled sac-like structure.

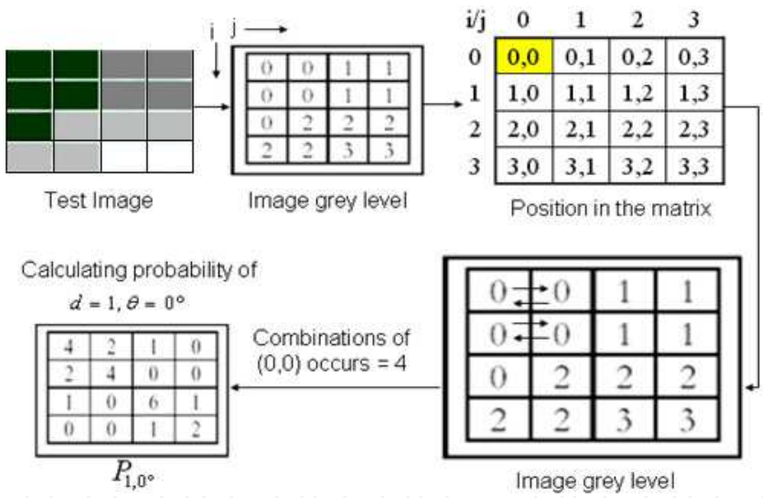


Fig. 5. Constructing SGLCM spatial matrix based on $\theta$ =0°, d=1, using 4 x 4 ROI block. Each pixel within the test image becomes the reference pixel of the position in the matrix of the direction of 0°. A reference pixel of 3 and its horizontal neighbour of 2 would contribute one count to the matrix element (3,2) and one count to the matrix element (2,3).

The spatial matrix, $P_{1,0^\circ}$ is constructed by filling in the probability of the combinations of pixels coordinate occurring in the window test image at the direction, denoted as angle, $\theta$. The top cell of $P_{1,0^\circ}$ will be filled with the number of times the combination of (0,0) occurs (i.e. amount of times within the image area a pixel with grey level 0 neighboring pixels) falls to the left and right side of another pixel with grey level 0 as the reference pixel. The number of combination of (0,0) that occurs are 4 at the angle direction of 0° with the distance, $d$=1. As such, the sparse matrix constructed corresponds to the size of the test image.

Similar calculations using SGLCM are evaluated with $\theta$=45°, 135°, 180°, 225°, 270°, and 315° as the direction of the reference pixel. If the test image is smaller (e.g 3 x 3 image block), the sum of all the entries in the SGLCM spatial matrix generated would be smaller.

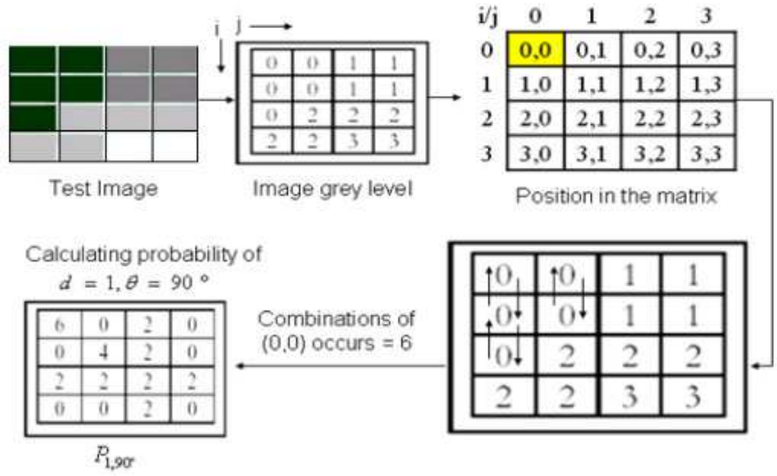


Fig. 6. Constructing SGLCM spatial matrix based on $\theta$ =90°, $d$=1, using 4 x 4 ROI block. A reference pixel of 0 and its neighbour of 0 at the direction of 90° will contribute one count to the matrix element (0,0). Similar to Fig. 4, a reference pixel of 3 and its vertical neighbour of 2 would contribute one count to the matrix element (3,2) and one count to the matrix element (2,3).

It is, in theory, possible to choose three or more pixels in a given direction [15]. However, this becomes extremely unwieldy for calculations and is not an operational procedure. Calculation involving three pixels would be third order, four pixels would be forth order and so forth.

### 4.1 Implementation of SGLCM for hepatic lesions using automated segmentation of the image block

An automated segmentation scheme using a flexible image block size for automated liver tissue characterization is shown in Fig. 7.

Square image blocks of widths of 5, 8 and 10 pixels were used within the liver boundary. The purpose of automated segmentation with these various block sizes was for preliminary diagnosis of the entire liver, without requiring intervention by the user in identifying an ROI.

### 4.2 Implementation and anlaysis

By using SGLCM, approximately two dozen co-occurrence features can be obtained [16]. Consideration of the number of distance angle relations also will lead to a potentially large number of dependent features. In this study, we restrict the representation to four features, which we hypothesize from Table 1 would provide useful information for texture characterization. These are entropy, correlation, contrast and homogeneity. For soft textures, the second order measurement distributions change very slightly with distance, while for coarse textures, the change in the distribution is rapid [16].

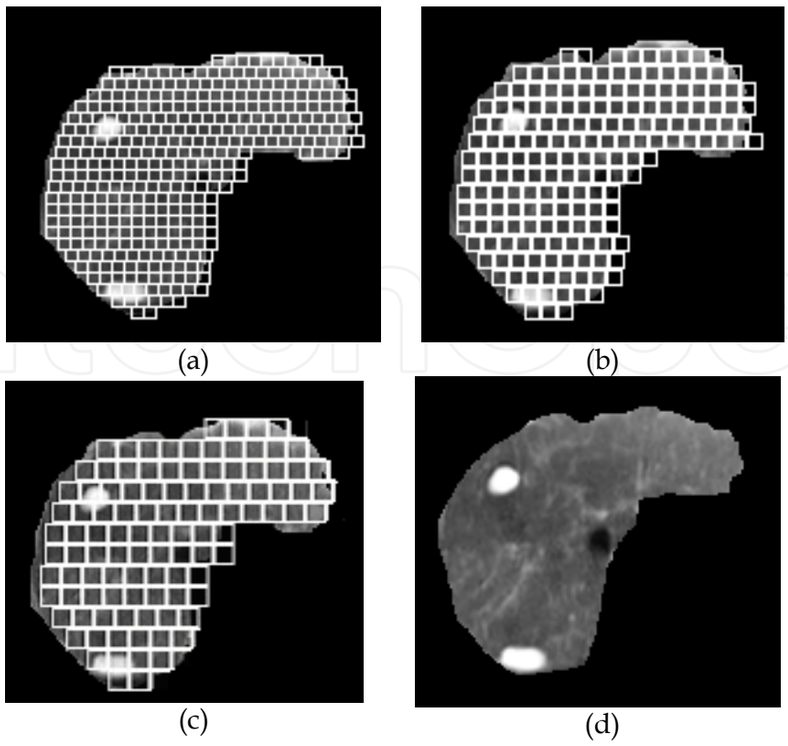


Fig. 7. Automated segmentation of image block in a cyst liver boundary using (a) 5 x 5 (b) 8 x 8 (c) 10 x 10 image block (d) shows the liver region in MRI abdomen image.

Table 2 shows the statistical results achieved for entropy calculated based on spatial co-occurrence matrices generated using SGLCM on cysts, tumor and healthy liver of the training set (*T1, T2, …, Tn*). Entropy is consistent within a specific range from 5.174-7.911 for cyst classification and 2.487- 4.291 for tumor classification. In healthy liver, entropy ranges from 0.054-1.954. As the entropy ranges are distinct for each of the 3 categories tested, entropy could be a suitable feature for successful liver lesions classification.

Table 3 provides the results for the correlation calculated using SGLCM. As observed, correlation is consistent within a specific range from 5.962-6.997 for cyst and 2.300-4.932 for tumor and 0.071-1.500 for healthy liver. Being different for the 3 categories, correlation may also be deemed a suitable classification feature.

The statistical results for two more features, homogeneity and contrast, calculated based on SGLCM on healthy liver ROI were inconsistent as shown in Table 4 and Table 5. As all the ranges for the 3 categories overlap, these features cannot be used to classify the liver MRI images.

### 4.3 Classification for hepatic lesions using neural networks and globus

The diagnostic value of MRI liver images has become increasingly important in liver disease detection. However, the interpretation effectiveness still relies heavily on experience and skill of the doctors. From the analysis of the SGLCM results obtained, only entropy and correlation are selected for classification for liver tumor and cyst.

| ROI | | Direction, $\theta$ | | | | Entropy | |
|---|---|---|---|---|---|---|---|
| | ROI | 0° | 45° | 90° | 135° | Min | Max |
| Cyst | T1 | 5.802 | 5.724 | 6.425 | 6.484 | 5.802 | 6.484 |
| | T2 | 5.487 | 5.524 | 5.925 | 6.183 | 5.487 | 6.183 |
| | T3 | 5.477 | 6.554 | 6.072 | 7.854 | 5.477 | 7.854 |
| | T4 | 5.339 | 6.774 | 6.241 | 7.692 | 5.339 | 7.692 |
| | T5 | 5.174 | 6.694 | 6.131 | 7.911 | **5.174** | **7.911** |
| | T6 | 5.477 | 5.884 | 6.082 | 7.054 | 5.477 | 7.054 |
| | T7 | 5.884 | 6.145 | 6.281 | 7.692 | 5.884 | 7.692 |
| Tumor | T8 | 2.802 | 2.724 | 2.925 | 4.284 | 2.802 | 4.284 |
| | T9 | 2.487 | 2.719 | 2.919 | 4.183 | **2.487** | 4.183 |
| | T10 | 2.677 | 2.794 | 2.999 | 4.254 | 2.677 | 3.254 |
| | T11 | 2.539 | 2.724 | 2.802 | 4.192 | 2.539 | 4.192 |
| | T12 | 2.494 | 2.894 | 2.994 | 4.291 | 2.494 | **4.291** |
| | T13 | 3.327 | 3.484 | 3.792 | 4.054 | 3.327 | 4.054 |
| | T14 | 3.124 | 3.145 | 3.381 | 4.102 | 3.124 | 4.102 |
| Healthy | T15 | 0.054 | 0.692 | 1.054 | 1.692 | **0.054** | 1.692 |
| | T16 | 0.082 | 0.281 | 1.082 | 1.954 | 0.082 | **1.954** |
| | T17 | 0.554 | 0.784 | 1.054 | 1.281 | 0.554 | 1.281 |
| | T18 | 0.887 | 0.231 | 1.607 | 1.784 | 0.887 | 1.784 |
| | T19 | 0.574 | 0.884 | 1.177 | 1.231 | 0.574 | 1.231 |
| | T20 | 0.114 | 0.145 | 1.484 | 1.884 | 0.114 | 1.884 |
| | T21 | 0.774 | 0.954 | 1.074 | 1.145 | 0.774 | 1.145 |

Table 2. Entropy results for cyst, tumor and healthy liver.

| ROI | | Direction, $\theta$ | | | | Correlation | |
|---|---|---|---|---|---|---|---|
| | ROI | 0° | 45° | 90° | 135° | Min | Max |
| Cyst | T1 | 5.962 | 6.403 | 6.825 | 6.854 | **5.962** | 6.854 |
| | T2 | 6.127 | 6.241 | 6.325 | 6.483 | 6.127 | 6.483 |
| | T3 | 6.493 | 6.554 | 6.610 | 6.854 | 6.493 | 6.854 |
| | T4 | 6.384 | 6.774 | 6.941 | 6.997 | 6.384 | **6.997** |
| | T5 | 6.128 | 6.694 | 6.910 | 6.111 | 6.128 | 6.910 |
| | T6 | 6.773 | 6.884 | 6.904 | 6.341 | 6.773 | 6.904 |
| | T7 | 6.237 | 6.345 | 6.431 | 6.562 | 6.237 | 6.562 |
| Tumor | T8 | 2.302 | 2.924 | 3.164 | 4.269 | 2.302 | 4.269 |
| | T9 | 2.300 | 2.811 | 3.119 | 4.702 | **2.300** | 4.702 |
| | T10 | 2.321 | 2.703 | 2.321 | 4.164 | 2.321 | 4.164 |
| | T11 | 2.370 | 2.718 | 3.860 | 4.718 | 2.370 | 4.718 |
| | T12 | 2.410 | 2.843 | 2.994 | 4.932 | 2.410 | **4.932** |
| | T13 | 3.156 | 3.481 | 3.494 | 4.156 | 3.156 | 4.156 |
| | T14 | 2.186 | 2.916 | 3.994 | 4.321 | 2.186 | 4.321 |
| Healthy | T15 | 0.110 | 0.241 | 1.314 | 1.500 | 0.110 | **1.500** |
| | T16 | 0.120 | 0.231 | 1.312 | 1.431 | 0.120 | 1.431 |
| | T17 | 0.152 | 0.214 | 1.224 | 1.322 | 0.152 | 1.322 |
| | T18 | 0.133 | 0.231 | 1.167 | 1.311 | 0.133 | 1.311 |
| | T19 | 0.142 | 0.284 | 1.437 | 1.410 | 0.142 | 1.410 |
| | T20 | 0.071 | 0.145 | 1.224 | 1.374 | **0.071** | 1.374 |
| | T21 | 0.140 | 0.254 | 1.284 | 1.350 | 0.140 | 1.350 |

Table 3. Correlation results for cyst, tumor and healthy liver.

| ROI | | Direction, $\theta$ | | | | Contrast | |
|---|---|---|---|---|---|---|---|
| | ROI | 0° | 45° | 90° | 135° | Min | Max |
| Cyst | T1 | 4.120 | 0.242 | 4.527 | 0.242 | 0.242 | 4.527 |
| | T2 | 0.872 | 10.51 | 2.520 | 11.21 | 0.872 | 11.21 |
| | T3 | 7.711 | 16.50 | 0.721 | 16.30 | 0.721 | 16.50 |
| | T4 | 0.091 | 7.741 | 2.411 | 17.41 | 0.091 | **17.41** |
| | T5 | 1.746 | 6.942 | 13.14 | 6.042 | 1.746 | 13.14 |
| | T6 | 14.01 | 5.841 | 0.821 | 0.841 | 0.821 | 14.01 |
| | T7 | 3.341 | 1.206 | 0.011 | 1.210 | **0.011** | 1.206 |
| Tumor | T8 | 0.103 | 0.212 | 0.527 | 0.242 | 0.103 | 0.527 |
| | T9 | 0.872 | 11.31 | 2.520 | 12.21 | 0.872 | 11.21 |
| | T10 | 0.001 | 17.20 | 0.761 | 13.40 | **0.001** | **17.20** |
| | T11 | 0.004 | 0.741 | 2.411 | 0.411 | 0.004 | 2.411 |
| | T12 | 0.246 | 6.842 | 8.104 | 0.052 | 0.052 | 8.104 |
| | T13 | 0.071 | 0.771 | 0.811 | 0.101 | 0.071 | 0.811 |
| | T14 | 1.345 | 1.216 | 0.081 | 1.210 | 0.081 | 1.345 |
| Healthy | T15 | 12.10 | 0.222 | 1.021 | 2.230 | 0.222 | 12.10 |
| | T16 | 3.212 | 0.141 | 12.02 | 11.21 | 0.141 | 12.02 |
| | T17 | 0.701 | 1.110 | 0.001 | 16.30 | **0.001** | **16.30** |
| | T18 | 1.091 | 0.011 | 2.017 | 12.41 | 0.011 | 12.41 |
| | T19 | 5.342 | 0.442 | 1.014 | 1.042 | 0.442 | 5.342 |
| | T20 | 1.121 | 5.821 | 0.123 | 10.31 | 0.123 | 10.31 |
| | T21 | 1.341 | 1.306 | 1.011 | 12.10 | 1.306 | 12.10 |

Table 4. Contrast Results for cyst, tumor and healthy liver.

| ROI | | Direction, $\theta$ | | | | Homogeneity | |
|---|---|---|---|---|---|---|---|
| | ROI | 0° | 45° | 90° | 135° | Min | Max |
| Cyst | T1 | 3.015 | 0.101 | 12.98 | 2.045 | 0.101 | 12.98 |
| | T2 | 5.178 | 1.087 | 0.251 | 1.101 | 0.251 | 5.178 |
| | T3 | 0.018 | 1.679 | 1.022 | 0.667 | 0.667 | 1.679 |
| | T4 | 10.54 | 12.05 | 11.02 | 1.668 | 1.668 | 12.05 |
| | T5 | 5.890 | 0.014 | 12.98 | 1.031 | 0.014 | **12.98** |
| | T6 | 0.012 | 11.02 | 0.023 | 0.098 | 0.012 | 11.02 |
| | T7 | 0.001 | 11.78 | 0.078 | 1.189 | **0.001** | 11.78 |
| Tumor | T8 | 0.040 | 1.212 | 5.527 | 2.142 | 0.040 | 5.527 |
| | T9 | 0.012 | 12.31 | 2.320 | 10.17 | 0.012 | 12.31 |
| | T10 | 0.007 | 11.30 | 12.61 | 13.24 | 0.007 | **13.24** |
| | T11 | 0.001 | 11.01 | 0.401 | 0.011 | **0.001** | 11.01 |
| | T12 | 11.20 | 0.047 | 10.14 | 0.009 | 0.009 | 11.20 |
| | T13 | 2.001 | 0.731 | 0.011 | 0.001 | **0.001** | 2.001 |
| | T14 | 2.562 | 3.691 | 0.001 | 0.001 | **0.001** | 3.691 |
| Healthy | T15 | 1.133 | 1.895 | 1.021 | 2.230 | 1.021 | 2.230 |
| | T16 | 0.112 | 0.141 | 6.027 | 11.21 | 0.112 | 6.027 |
| | T17 | 0.001 | 0.140 | 0.001 | 12.31 | **0.001** | 12.31 |
| | T18 | 0.001 | 0.011 | 2.028 | 0.480 | **0.001** | 2.028 |
| | T19 | 11.30 | 0.442 | 1.134 | 0.001 | **0.001** | 11.30 |
| | T20 | 12.01 | 0.821 | 0.123 | 2.078 | 0.123 | 12.01 |
| | T21 | 0.001 | 0.002 | 1.011 | 13.28 | **0.001** | **13.28** |

Table 5. Homogeneity results for cyst, tumor, and healthy liver.

The texture features obtained were then applied to the NN classifier and Globus automated scheduling for the detection. The final decisions of the NN classifier was generated by combining the diagnostic output using the input layer consisting of a number of input neurons equal to the number of features fed into the NN. (i.e. 2, namely entropy and correlation. Training and testing of the NN classification was based on the use of sample MRI abdomen images for all 3 categories as observed in Table 6.

| | Entropy | | Correlation | |
|---|---|---|---|---|
| | Min | Max | Min | Max |
| Cyst | 5.174 | 7.911 | 5.962 | 6.997 |
| Tumor | 2.487 | 4.291 | 2.300 | 4.932 |
| Healthy | 0.054 | 1.954 | 0.071 | 1.500 |

Table 6. Classification of hepatic lesions using entropy and correlation.

## 5. Conclusion

In the approach described above, it should be noted that, resolution, ROI image block size and sampling space used for calculation of SGLCM are important considerations in statistical feature extraction. The present study has shown promising results in the use of texture for the extraction of diagnostic information from MR images of the liver. Two features were selected using SGLCM, namely entropy and correlation, whilst it was shown that homogeneity and contrast were unsuitable to differentiate between cyst, tumor and healthy liver. In our experiment, the same features were used as input to the NN with the aid of Globus automated scheduling for hepatic liver tissue characterization of MRI images. In particular, this paper provides results of successful preliminary diagnosis of cyst and liver tumor in the liver tissue.

## 6. References

[1] Carrillo, J. L. Duerk, J. S. Lewin, D. L. Wilson, "Semiautomatic 3-D image registration as applied to interventional MRI liver cancer treatment." *IEEE Transactions on Information Technology in Biomedicine*, vol. 19, pp. 175-185, 2000.

[2] M. Gletsos, S. G. Mougiakakou, G. K. Matsopoulus, K. S. Nikita, A. S. Nikita and D. Kelekis, "A Computer-aided Diagnostic System to Characterize CT Focal Liver Lesions: Design and Optimization of a Neural Network Classifier", *IEEE Transactions on Information Technology in Biomedicine*, vol. 7, no. 3, pp. 153-162, 2003.

[3] S. Kitaguchi, S. Westland and M. R. Luo, "Suitability of Texture Analysis Methods for Perceptual Texture", Proceedings, *10th Congress of the International Colour Association*, vol. 10, pp. 923-926, 2005.

[4] Valanis, S. G. Mougiakakou, K. S. Nikita and A. Nikita, "Computer-aided Diagnosis of CT Liver Lesions by an Ensemble of Neural Network and Statistical Classifiers", *Proceedings of IEEE International Joint Conference on Neural Networks,* vol. 3, pp. 1929-1934, 2004.

[5] E. L. Chen, P. C. Chung, C. L. Chen, H. M. Tsai and C. L. Chang, "An automatic diagnostic system for CT liver image classification", *IEEE Transactions on Biomedical Engineering*, vol. 45, no. 6, pp. 783-794, 1996.

[6] H. Mir, M. Hanmandlu and S. N. Tandon, "Texture Analysis of CT Images", *IEEE Transactions on Computers*, vol. 42, no. 4, pp. 501-507, 1993.

[7] S. G. Mougiakakou, I. Valanis, K. S. Nikita, A. Nikita and D. Kelekis, "Characterization of CT Liver Lesions Based on Texture Features and a Multiple Neural Network Classification Scheme", *Proceedings of the 25th Annual International Conference of the IEEE EMBS*, vol. 2, no. 3, pp. 17-21, 2001.

[8] D. Goldberg, "Genetic Algorithms in Search, Optimization and Machine Learning", *Addison-Wesley*, 1989.

[9] Julesz, "Experiments in the Visual Perception of Texture", *Scientific American*, vol. 232, no. 4, pp. 34-43, 1975.

[10] Materka and M Strzelecki, "Texture Analysis Method-A Review", *COSTB11 Report*, pp. 1-33, 1998.

[11] G. D. Kendall and T. J. Hall, "Performing fundamental image processing operations using quantized neural networks", *International Conference on Image Processing and its Applications*. vol. 4, no. 1, pp. 226-229, 2002

[12] R. Haralick, "Statistical and Structural Approaches to Texture", *Proceedings of IEEE*, vol. 67, no. 5, pp. 786-804, 1979.

[13] Kyoung, "An Adaptive Resource-Allocating Network for Automated Detection, Segmentation, and Classification of Breast Cancer Nuclei Topic Area", *Image Processing and Recognition, Neural Networks*, Israel, 2003.

[14] L.L Lanzarini, A.C. Camacho, A. Badran and D. G. Armando, "Images Compression for Medical Diagnosis using Neural Networks", *Processing and Neural Networks*, vol. 10, no. 5, pp. 13-16, 1997.

[15] Lauterbach, "A Neural Network Based Recognition of Complex Two-Dimensional Objects", *IEEE Transaction on Computers*, vol. 1, no.6, pp. 203-210, 1996.

[16] S. I. Kim, K. C. Choi and D. S. Lee, "Texture classification using run difference matrix", *Proceedings of Ultrasonics Symposium,* vol. 2, no. 10, pp. 1097-1100, 1991.

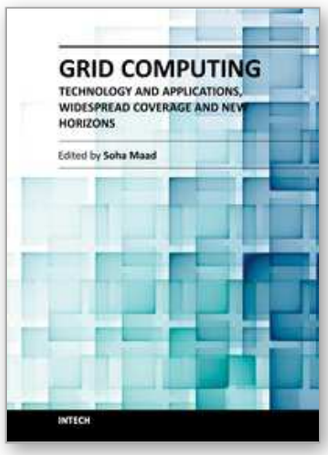


**Grid Computing - Technology and Applications, Widespread Coverage and New Horizons**

Edited by Dr. Soha Maad

ISBN 978-953-51-0604-3
Hard cover, 354 pages
**Publisher** InTech
**Published online** 16, May, 2012
**Published in print edition** May, 2012

Grid research, rooted in distributed and high performance computing, started in mid-to-late 1990s. Soon afterwards, national and international research and development authorities realized the importance of the Grid and gave it a primary position on their research and development agenda. The Grid evolved from tackling data and compute-intensive problems, to addressing global-scale scientific projects, connecting businesses across the supply chain, and becoming a World Wide Grid integrated in our daily routine activities. This book tells the story of great potential, continued strength, and widespread international penetration of Grid computing. It overviews latest advances in the field and traces the evolution of selected Grid applications. The book highlights the international widespread coverage and unveils the future potential of the Grid.



INTECH
open science | open minds

**InTech Europe**
University Campus STeP Ri
Slavka Krautzeka 83/A
51000 Rijeka, Croatia
Phone: +385 (51) 770 447
Fax: +385 (51) 686 166
www.intechopen.com

**InTech China**
Unit 405, Office Block, Hotel Equatorial Shanghai
No.65, Yan An Road (West), Shanghai, 200040, China
中国上海市延安西路65号上海国际贵都大饭店办公楼405单元
Phone: +86-21-62489820
Fax: +86-21-62489821

IntechOpen